

Observations of the spectral clear-sky aerosol forcing over the tropical Indian Ocean

Jens Meywerk and V. Ramanathan

Center for Clouds, Chemistry, and Climate, Scripps Institution of Oceanography
University of California, San Diego, La Jolla

Abstract. During the first field phase (FFP) of the Indian Ocean Experiment (INDOEX) in February and March, 1998, the spectral global and direct beam irradiance have been measured between 350 and 1050 nm wavelengths using a 512-channel, fixed grating, photodiode array spectroradiometer. A detailed analysis of the instrument's reliability, the absolute calibration, and the corrections for deviation from the ideal cosine response are presented. For most of the spectral region the total uncertainty is shown to be $<2\%$. The spectral optical depth, the spectral aerosol forcing, and the aerosol forcing for the photosynthetically active radiation have been derived from direct beam measurements and global irradiance measurements. The optical depth at 500 nm wavelength decreases from ~ 0.5 in the northern Arabian Sea to as low as 0.05 south of the Intertropical Convergence Zone (ITCZ) near $\sim 15^\circ\text{S}$ latitude. The surface aerosol forcing efficiency is defined as the rate of change of net irradiance at the surface due to an increase by 1 in optical depth at 500 nm. The normalization procedure we adopt to determine the aerosol forcing efficiency with respect to a reference pristine day in the Southern Hemisphere eliminates most of the radiometric calibration uncertainties. The continental aerosol south of the ITCZ shifts the peak in the direct solar radiation from 470 nm (for pristine conditions) to ~ 580 nm for the polluted region. The spectral aerosol forcing efficiency peaks around 460 nm, with -1.2 , -0.6 , and $+0.6 \text{ W m}^{-2} \text{ nm}^{-1}$ for the direct, global, and diffuse irradiance, dropping for the lower and higher wavelengths to about -0.3 , -0.25 , and $0.05 \text{ W m}^{-2} \text{ nm}^{-1}$ at 350 nm and -0.3 , -0.1 , and $+0.2$ at 1050 nm. Integrated over 400–700 nm, the aerosols decrease the noontime solar flux by as much as -38 W m^{-2} in the Arabian Sea to as little as -2 W m^{-2} south of the ITCZ. This introduces a strong north to south gradient in the climate forcing of the ocean. In addition, the strong aerosol modulation of the photosynthetically active radiation (400–700 nm) and its north to south gradient have important implications for biomass production of the ocean.

1. Introduction

Two of the major remaining uncertainties in determining climate change from global circulation models are the poorly understood aerosol-radiation interactions and the magnitude of the aerosol forcing at the surface, i.e., the change in net solar irradiance due to an increase in the aerosol columnar optical depth [Intergovernmental Panel on Climate Change (IPCC), 1995]. The greenhouse gases are known to trap heat in the atmosphere by decreasing the outgoing longwave radiation, thus having a warming effect on the climate system. Aerosols may have both effects, warming or cooling, by changing the optical properties of the atmosphere (scattering and absorption), in cloudless or cloudy conditions. The former is called the direct effect, whereas a change in the cloud microphysical properties by aerosol particles is referred to as the indirect aerosol effect. Aerosols are not uniformly distributed throughout the globe, and their radiative forcing is strongly dependent on the geographical location on Earth [Kiehl and Briegleb, 1993].

This paper focuses on the direct aerosol effect on the solar radiation budget at the sea surface; in particular, we consider

two quantities: (1) aerosol forcing, which is defined as the effect of the aerosol on the net (direct and diffuse) irradiance at the surface and (2) surface aerosol forcing efficiency, which is defined as the rate of change of the net irradiance per unit increase in the aerosol optical depth.

One of the best regions to investigate the aerosol forcing is the Indian Ocean during the winter monsoon season, when low-level transport of highly polluted air from India to the Arabian Sea and the adjacent Indian Ocean can be observed [Pham *et al.*, 1995; V. Ramanathan *et al.*, unpublished data, 1996]. Measurements from south of the Intertropical Convergence Zone (ITCZ) can provide the offset for the natural aerosol's influence on the radiation budget, because of the lack of industrial activity around the central and southern Indian Ocean area. Furthermore, the intertropical convergence zone acts like a barrier for air mass exchange between the two hemispheres. The climatological mean ITCZ is located between 0° and 10°S during February and April. Hence the best approach is to carry out measurements on both sides of the ITCZ in order to get the aerosol radiative properties for both air masses: the clean southern Indian Ocean air and the highly polluted air from the Indian subcontinent over the Arabian Sea (V. Ramanathan *et al.*, unpublished data, 1996).

To determine the direct aerosol forcing, it is necessary to measure the aerosol optical depth at a certain wavelength (500 nm) and correlate this with the global solar flux measured at

Copyright 1999 by the American Geophysical Union.

Paper number 1999JD900502.
0148-0227/99/1999JD900502\$09.00

the sea surface. The global flux or global irradiance is defined as the direct solar beam plus the diffuse irradiance penetrating a horizontal surface. Integrated over the entire solar spectral range, the global irradiance is the total solar energy reaching the Earth's surface: one of the most important energy parameters of the climate system.

The main question that we address in this paper is the following: How do aerosols modulate the solar radiative flux at the sea surface? There are a few papers addressing this issue by using direct broadband measurements [Jayaraman *et al.*, 1998; Krishna Moorthy *et al.*, 1998], but none of them addresses the problem with high spectral resolution over $\sim 60\%$ of the solar spectrum. This paper provides, perhaps for the first time, the spectral dependence of the aerosol forcing. Furthermore, this paper also provides direct measurements of the north-south gradient in the aerosol forcing.

2. Experimental Setup

We used a 512-channel, fixed grating spectroradiometer measuring the spectral, global irradiance and direct-normal irradiance at the sea surface between 350 and 1050 nm with a resolution of 3 nm. This kind of spectroradiometer (Analytical Spectral Devices, Inc. (ASD) FieldSpec VNIR) was intended to be used primarily for deriving spectral reflectance from natural surfaces in order to get satellite ground truth and for chemical spectral analyses. Our major concern was the reliability of the measurements and the instrument's absolute calibration. A detailed technical description of the basic features of the instrument can be found in the instrument's manual [Curtiss and Goetz, 1997]. The instrument has been used during the April 1996 Atmospheric Radiation Measurement Program (ARM) Southern Great Plains Cloud and Radiation Testbed (CART) site intensive observation period [Pilewskie *et al.*, 1998].

The spectroradiometer was mounted on board the Indian ORV *Sagar Kanya* (cruise 133), and was operated during the entire first field phase of the Indian Ocean Experiment (INDOEX). One of the major goals of INDOEX is to get a better understanding of the aerosol composition and distribution over the Arabian Sea and the Indian Ocean region, as well as the latitudinal changes and the impact of aerosols on the solar radiative transfer. The results are expected to provide better parameterization of aerosol forcing for climate modeling. A detailed description of the experiment and its goals are given by V. Ramanathan *et al.* (unpublished data, 1996), and details of the first field phase are given by H. V. Nguyen *et al.* (unpublished data, 1998).

Figure 1 shows the cruise track through the Indian Ocean with the noontime aerosol forcing and aerosol optical depth $\Delta\tau$ written next to the track. The small insert displays the Julian day. All data measured inside the exclusive economic zones (EEZs) of India and Mauritius had to be excluded because of pending clearance from the Government of India.

The instrument was set up to measure the global or direct irradiance. The continuous measurements of the global irradiance (one spectrum every 40 s) had to be interrupted frequently for ~ 3 min each time to measure the direct irradiance, from which the spectral optical depth was derived. During each of these 3 min interruptions, 100 spectra of the direct solar beam were taken. For this purpose the receiving element for the 2π field of view (FOV) for global irradiance was covered with a pipe, narrowing its FOV from 180° to 2° . With the help of a pointing device it was possible to point this pipe directly

into the solar beam. The direct beam measurements had to be handheld, since there is no way, on a pitching, rolling, and turning ship, to point the receptor to the solar disc automatically. An average of 10 spectra with the largest irradiances at 500 nm was assumed to represent the true direct irradiance. These direct measurements were carried out for a variety of solar zenith angles between 0° and 80° and on both sides of the Equator, whenever the solar disc was not obstructed by clouds. Figure 2 shows a typical time series of a direct beam measurement event for the 500 nm channel. The 10 highest values are marked as big shaded squares. Their standard deviation is only 0.13%.

The receiving element for measuring the global irradiance was mounted on a gimbal in order to minimize the influence of the ship's motion on the signal. Horizontal accelerations of the ship due to turns, however, are not compensated for and might result in a slight tilt of the sensor's surface. The remaining tilt of the diffuser is estimated to be $<5^\circ$. Since this kind of movement is periodically and randomly distributed in both directions, any remaining tilt of the sensor's surface will be averaged out. The gimbal post had been welded to the rail on the foredeck of the ship. It turned out that this location was the very best for the hemispherical irradiance measurements on the ship. Plate 1 shows the hemispherical view from the ASD gimbal. The obstruction from the ship as well as a possible influence of the stack gases of the ship are minimal for this spot. The mast on the foredeck and the radome on top of the ship are the worst obstructions "seen" by the spectroradiometer. The area in Plate 1 is directly proportional to the cosine-weighted influence on the irradiance, since it is a projection linear in the cosine of the solar zenith angle.

3. Reliability of Measurements and Calibration

The most critical issues for the spectral measurements are the following: (1) zero offset of the instrument, (2) absolute calibration, and (3) deviation from an ideal cosine response of the light-receiving diffuser.

The dark current or zero offset is defined as the signal that appears when there is no light entering the spectroradiometer. The ASD spectroradiometer offers the opportunity for taking these zero-offset measurements on a regular schedule and subtracts the zero offset from the signal automatically. For this purpose the light entrance to the silicone diode array is shut, and the reading for the dark offset is taken. The zero offset (one for each channel) is stored in memory and is subtracted from the next measurement until the next zero offset is read again. The zero offset basically originates from thermal electrons in the detector material, and this signal is temperature dependent. The zero-offset problems have been minimized by mounting the instrument inside a temperature-controlled enclosure and by taking spectral dark current measurements once every minute. The temperature was controlled using two regulated, high-capacity thermoelectric elements.

The absolute calibration of the radiometer was checked almost every day using a LI-COR optical calibrator. This calibration is basically a wavelength by wavelength comparison of the readings of the spectroradiometer with a secondary National Institute of Standards and Technology (NIST) standard lamp with known spectral emission at a known distance from the source. The calibrator's manufacturer states a 3% uncertainty for this kind of calibration [LI-COR, 1990]. In a recent study (J. J. Michalsky *et al.*, unpublished data, 1998) an even

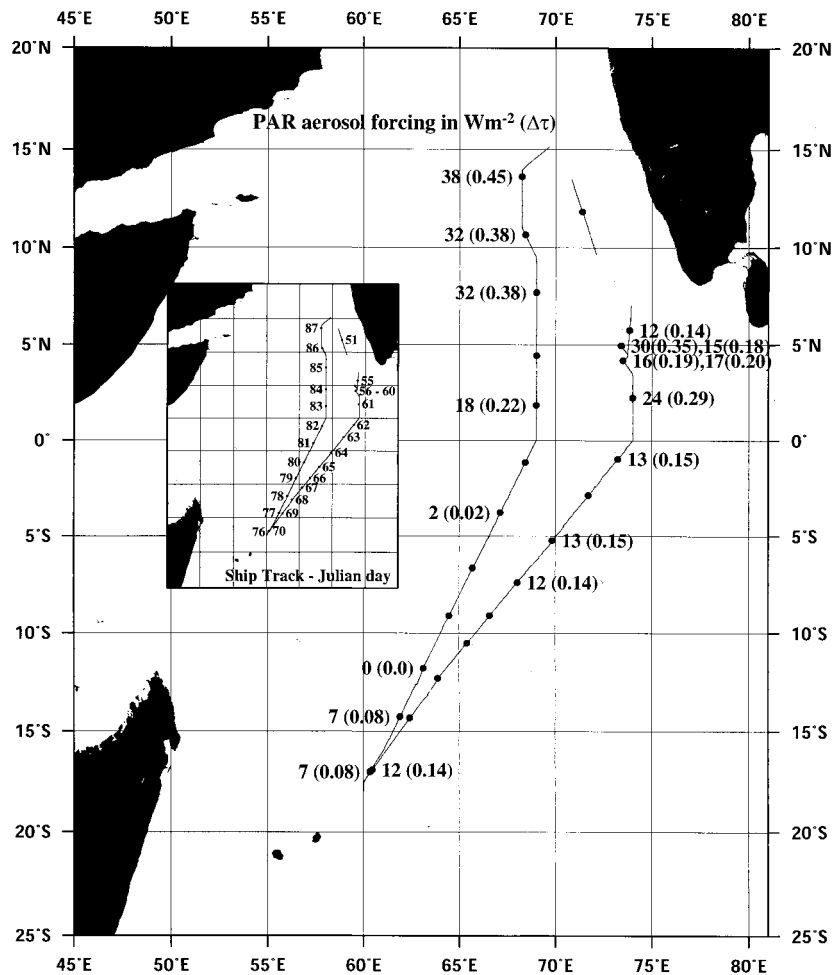


Figure 1. Cruise track of the *Sagar Kanya* cruise 133, during the first field phase 1998 of INDOEX, with noontime aerosol forcing in the 400–700 nm region and $\Delta\tau$. The numbers on the left-hand side of the track are the aerosol forcing for the photosynthetically active radiation (PAR) channel (400–700 nm) in W m^{-2} ; numbers in parentheses are aerosol optical depth $\Delta\tau$ relative to reference day 78 (March 19, 1998). Numbers next to the track on the insert map are day since January 1, 1998.

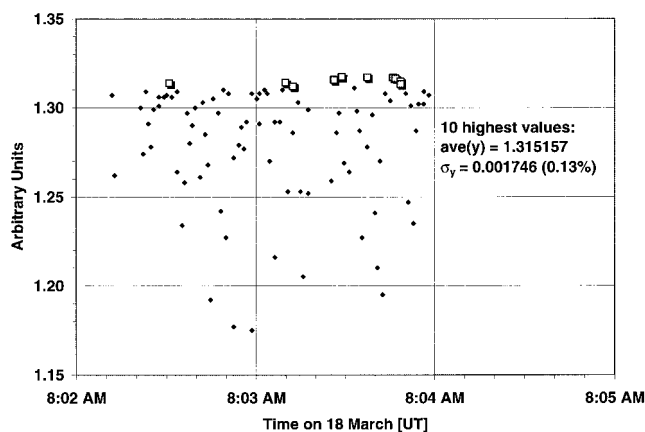


Figure 2. Time series of a typical handheld direct measurement event with the average for the 10 highest values and its standard deviation σ_y . Examples shows direct measurement from March 18, 1998.

smaller uncertainty of $<2\%$ was found for this type of calibration, comparing different standard lamps and calibrators. A time series of the calibration coefficients at different wavelengths from the entire cruise is shown in Figure 3. The time series displays the average calibration constants as derived for each calibration during the experiment. Each data point represents an average over 200 spectra taken during each calibration process. The drift observed is ~ 1000 times less than the variability of the average constants. Hence the instrument is very stable with time. A set of average calibration constants (an average over all individual calibrations performed during the experiment, one constant for each wavelength band) could be used for the entire data set.

The relative uncertainty of each of these calibration constants during the individual calibrations is shown in Figure 4. It is the standard deviation in percent for the 200 spectra taken during each individual calibration. Basically, the uncertainties of each of the individual calibrations are well below 1% for all wavelengths and are as good as 0.1% near 550 nm.

The total uncertainty using an average of all individual calibrations done in the field is displayed in Figure 5. This measure of uncertainty includes the day-to-day variability as can be

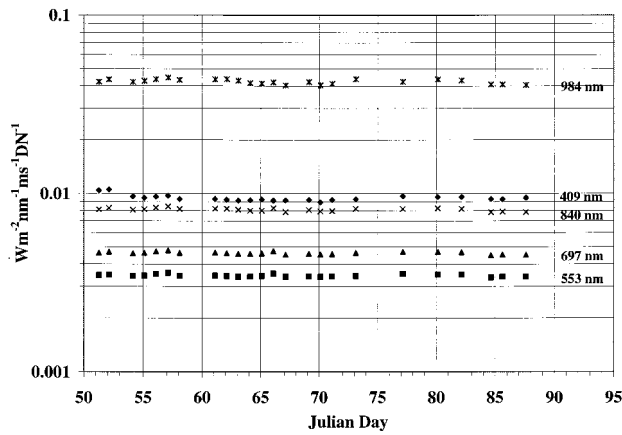


Figure 3. Time series of calibration constants for five different wavelengths and for each calibration done during the experiment. DN, digital number.

seen from Figure 3, as well as the variability during the individual calibrations themselves (Figure 4). Figure 5 is a measure of the total wavelength-dependent uncertainty in the data. For most of the spectral region the uncertainty was found to be below 2% (500–950 nm), which is of the same order of magnitude as for the calibration lamp itself. The reason for the increasing uncertainty at short and long wavelengths is given below. At short wavelengths the primary cause is low quantum efficiency of the detector and the low signal. The fact that the LI-COR lamp used during calibration has a relatively low color temperature of 3200 K with resulting steepness of the curve to shorter wavelengths adds onto the aforementioned uncertainty. This steepness results in a lamp output very sensible to voltage changes, in spite of the well-regulated power supply in the LI-COR calibrator. For the longer wavelengths the quantum efficiency of the detector is temperature dependent and decreasing with increasing wavelength. Since the instrument was temperature stabilized, it is obvious that the uncertainty in the longer wavelengths is originating from the decreasing quantum efficiency of the silicone detector.

For measuring the hemispheric irradiance (the global irradiance) a Delrin diffuser is used to receive the radiation from all angles of the hemisphere the diffuser is pointed to. In an ideal case, direct and diffuse radiation from all angles above

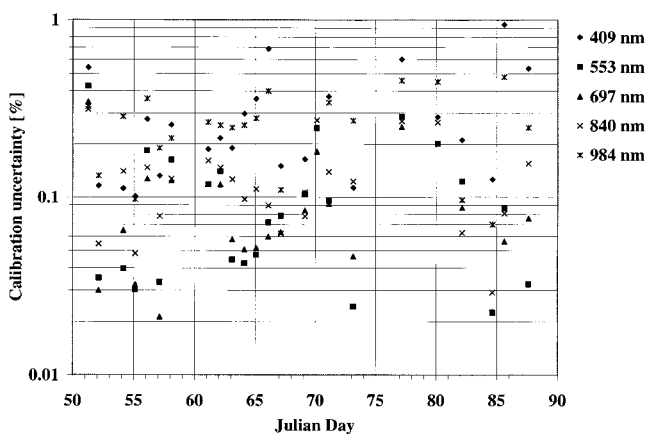


Figure 4. Relative uncertainty (in percent) associated with each of the calibrations done during the experiment.

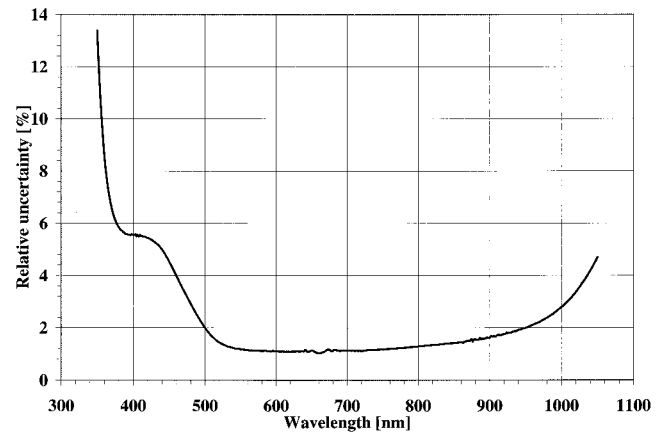


Figure 5. Wavelength-dependent total uncertainty in percent associated with using an average calibration for the entire cruise.

the diffuser's surface are isotropically scattered through the Delrin diffuser and weighted by the cosine of its angle of incidence. However, even very high quality diffusers do not behave like an ideal diffuser: The energy detected by the instrument still depends on the angle of incidence. The deviation from an ideal cosine response of this particular diffuser was checked right before the equipment was sent out to the cruise. Since the absolute calibration is done for normal incidence only, the relative deviation (relative to normal incidence) from an ideal cosine response needed to be known. Figure 6 displays the azimuthally averaged cosine response error of the diffuser for seven different wavelengths. The diffuser tends to increasingly overestimate the radiation with increasing zenith angle, with a maximum of $\sim 12\%$ at 55° zenith angle and 600 nm wavelength, dropping rapidly to an underestimation of $\sim 20\%$ at 80° . The effect of the cosine response error (Figure 6) was minimized by correcting the global radiation with a cosine response factor (see detailed derivation of this factor in the appendix).

An example of the global, direct, and diffuse spectral irradiances is shown in Plate 2 for the most pristine day (day 78, March 19, 1998, $\sim 12^\circ\text{S}$) south of the ITCZ and the most

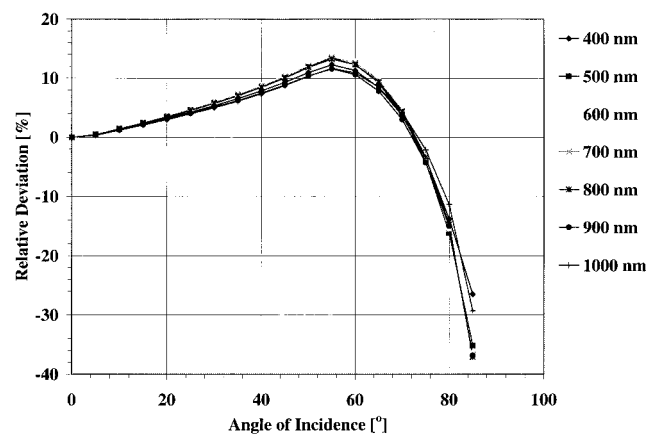


Figure 6. Relative deviation of the diffuser's response from an ideal cosine rule, azimuthally averaged, for seven different wavelengths spread throughout the ASD spectroradiometer spectrum.

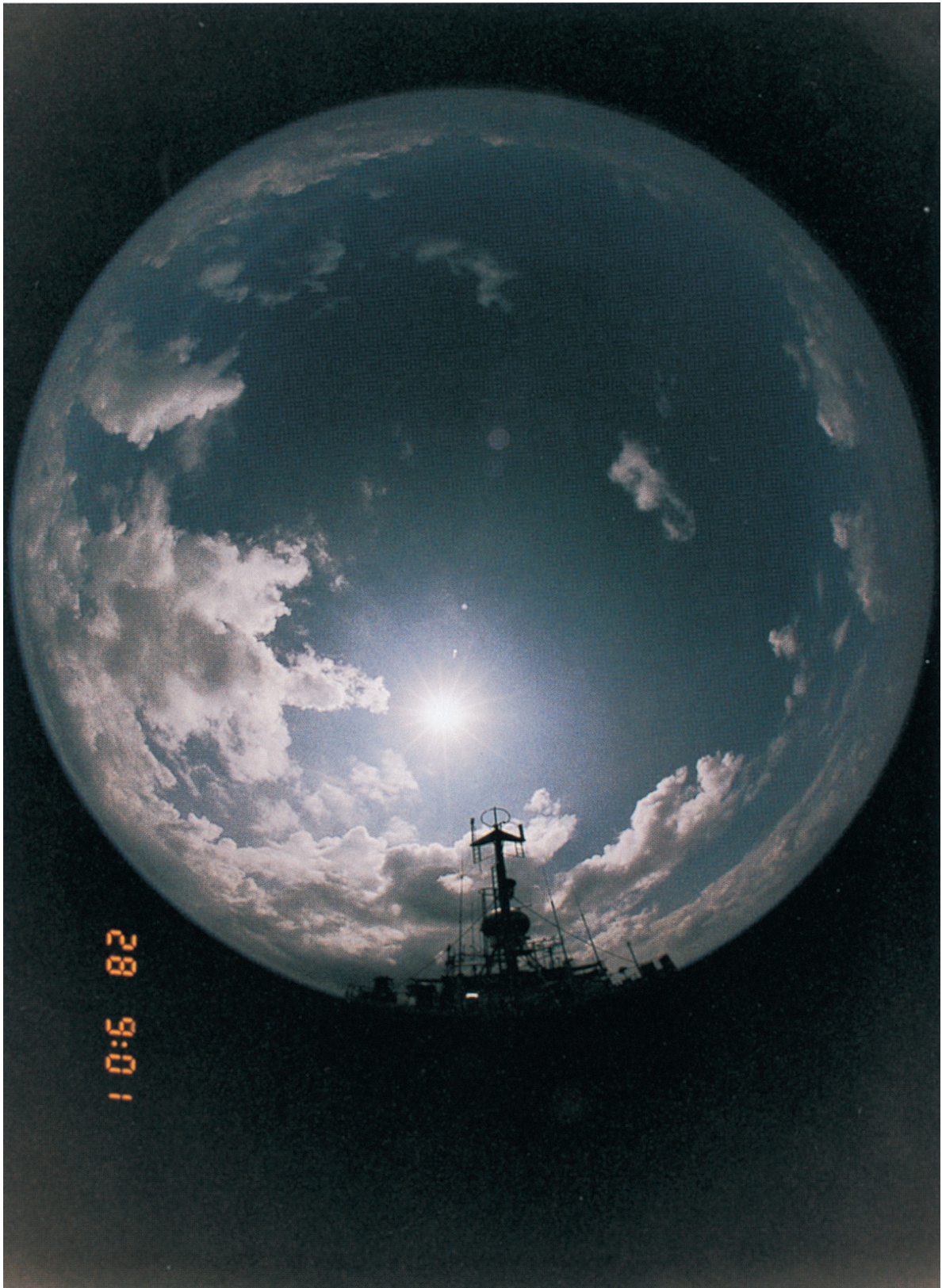


Plate 1. 2π view of the receiving element, the diffuser, of the Analytical Spectral Devices, Inc. (ASD) spectroradiometer from the rail of the foredeck on the Sagar Kanya.

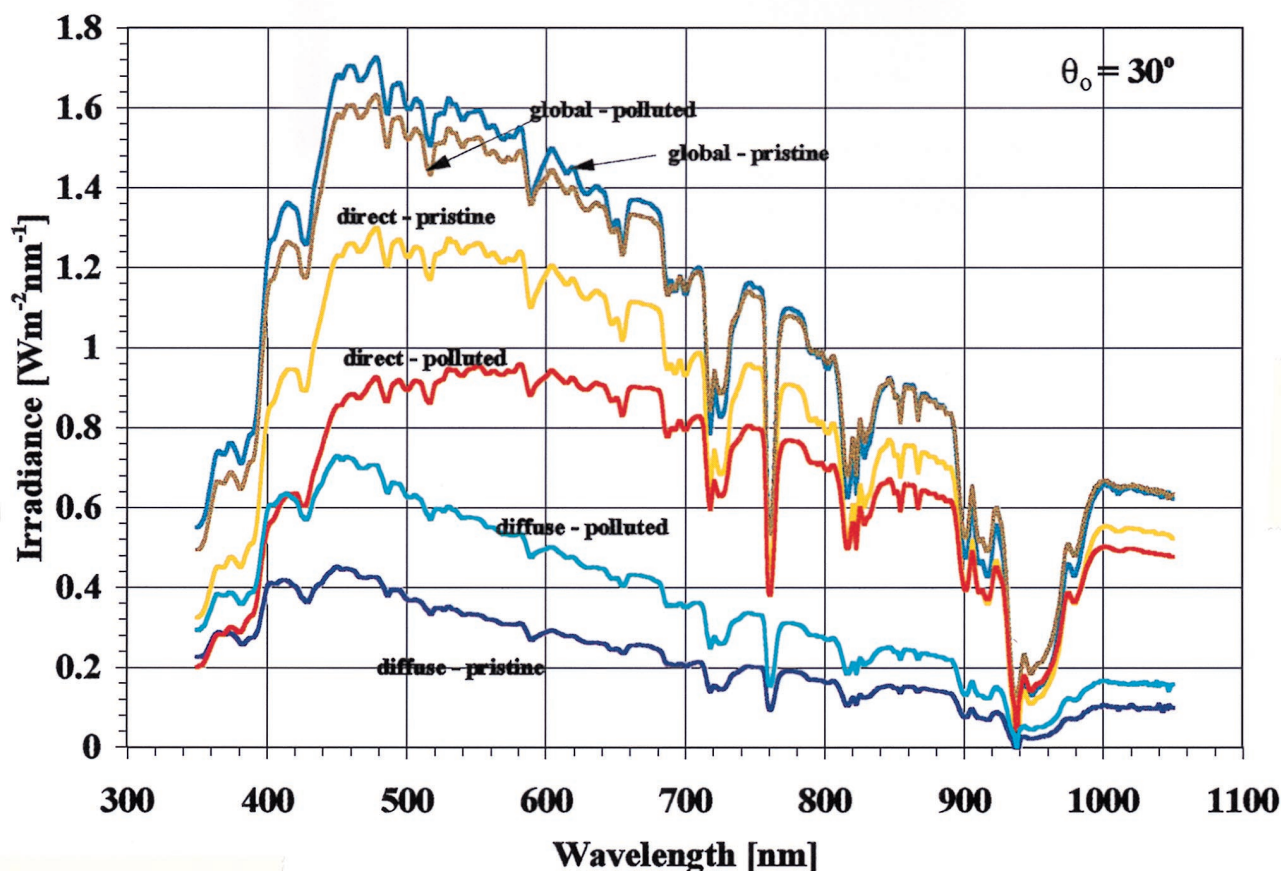


Plate 2. Global, direct, and diffuse portion of the spectral irradiance for the most pristine day, day 78 (March 19, 1998) at $\sim 12^{\circ}\text{S}$, and the most polluted day, day 85 (March 28, 1998) at $\sim 8^{\circ}\text{N}$. Solar zenith angle for both samples was 30° .

polluted day (day 85, March 26, 1998, $\sim 8^{\circ}\text{N}$) after all corrections were applied to the data. The diffuse irradiance was determined as the difference between global and direct beam measurements and hence is not an independent measurement. For both cases shown here, the solar zenith angle was 30° .

A reduction of the global radiation by $\sim 10\%$ can be seen in the wavelength band between 450 and 500 nm, due to the enhanced aerosol load. The direct portion of the solar spectrum is reduced by $\sim 25\%$, whereas the diffuse irradiance is increased by $\sim 60\%$ when the aerosol load increases. As is known, the major influence of the aerosols is in redistributing radiation from the direct beam into the diffuse skylight by Mie scattering. One part of this scattered radiation is scattered back to space; a bigger part is scattered to the Earth's surface, increasing diffuse skylight, since aerosol particles tend to show a strong forward scattering peak, depending on their size. The balance, depending on the amount of dust and soot particles, is absorbed by the aerosols. Hence, for illumination from the upper hemisphere, most of the light is scattered down to the Earth's surface.

Besides the changes in magnitude of the different parts of the global radiation, a shift in the wavelength of maximum intensity is also observed. The maximum intensity wavelength for the direct beam is at ~ 470 nm for the most pristine day, whereas the corresponding value for the most polluted day is at 580 nm. That means a stronger influence of the aerosol extinction in the shorter wavelengths. The maximum intensity for the diffuse irradiance is at 450 nm for both cases. This very short

wave maximum is a result of the Rayleigh scattering which dominates the diffuse skylight.

4. Deriving Optical Depth From Measurements

Our fundamental interest in this study is in the change in the surface solar irradiance in response to a change in the aerosol optical depth $\Delta\tau$. Our reference τ is taken to be that for the most pristine day during the cruise, i.e., the lowest value of τ observed during the cruise. This does not necessarily mean that there are no aerosols on the reference day, but rather that we expect the most pristine day to be very close to an undisturbed marine environment with respect to anthropogenic aerosol load. The difference in the solar fluxes between this reference day and any other day yields the effect of aerosol increase (from the reference value) on the solar fluxes, i.e., the aerosol forcing. The aerosol forcing, so defined, is not necessarily solely due to anthropogenic aerosols, for changing wind speeds can lead to changes in sea-salt optical depth. Since we have largely been in regions with very low winds during the entire cruise, changes in sea-salt aerosols do not contribute to $\Delta\tau$. The aerosol forcing yielded by our measurements largely reflects forcing due to aerosols with continental sources, particularly the Indian, Sri Lankan, and Indochinese regions. Not all of these aerosols, however, are anthropogenic; desert dust also contributes to the aerosol burden [Jayaraman *et al.*, 1998].

This approach of correlating $\Delta\tau$ (instead of τ) with changes in solar fluxes (instead of the fluxes) has the advantage of

reducing any residual uncertainty associated with the absolute calibration of the instrument, since $\Delta\tau$, as shown below, is relatively insensitive to the uncertainty in the extraterrestrial solar irradiance. Furthermore, as shown below, there is also no need to correct for changes in ozone absorption and Rayleigh extinction or for uncertainties resulting from the 2° field of view instead of a 0.5° field of view (which is the size of the solar disc) during the direct beam measurements.

In order to calculate the aerosol optical depth from the direct measurements, we calculated the Rayleigh and ozone optical depth (where applicable) and subtracted these values from the total optical depth (aerosols, molecular scattering, and absorbers like water vapor and ozone) derived from the direct beam measurements. The Rayleigh optical depth was calculated by using a wavelength and surface pressure-dependent parameterization for the Rayleigh optical depth calculation. The Rayleigh optical depth is affected by the total air column above the surface, which is correlated to the surface pressure. Since the Rayleigh optical depth at any given wavelength is linearly dependent on the ratio between actual pressure and standard pressure, an increase in surface pressure from the standard pressure of 1013.5 hPa (which we assumed for the surface pressure at all times) to an extreme value of 1025 hPa would only lead to an increase in Rayleigh optical depth of 1.16%. Furthermore, since the Rayleigh optical depth contributes between 10% and 75% of the total optical depth (depending on the spectral region and the aerosol optical depth), the absolute uncertainty introduced by day-to-day variations in Rayleigh optical depth due to changes in surface pressure is well below 1% for the worst case at shorter wavelengths.

From ozone column content measurements (Microtops II Ozonemonitor), which have been made during the entire cruise, the ozone column content varied from 230 Dobson units (DU) inside the ITCZ to 250 DU well north and south of the ITCZ. This leads to an uncertainty of 4% in the calculation of the ozone optical depth in the peak of the Hartley band. However, if you take into account that the total ozone optical depth is only 10% of the total optical depth in that particular band, the uncertainty in aerosol optical depth calculation due to changes in ozone column content is only 0.4%.

The last major uncertainty is in using the 2° field of view for the direct solar measurement instead of using a 0.5° field of view. We estimate the magnitude of this uncertainty in the following paragraphs.

We constructed two cases which we assume to be the extreme scenarios for our data set. To estimate the influence of the forward scattering peak on the spectral direct beam irradiance we need to make an assumption about the spectral optical depth and the scattering phase function. We consider two extreme cases:

The first case consists of very large, nonabsorbing particles with a very strong forward scattering peak but weak wavelength dependency, which would be typical for sea-salt particles in coarse mode. We assumed a spectral optical depth of the following kind: 0.3, 0.25, 0.25, and 0.2 at the respective wavelengths 300, 500, 700, and 900 nm. The phase function is from Köpke *et al.* [1997] for a coarse sea-salt (SSCM) component. From the optical depth we get an estimate of the amount of radiation scattered into the entire sphere around the particle, which, for this case, is 26%, 22%, 22%, and 18% for the respective wavelengths. After integrating the phase function over the forward peak from 0.5° to 2° , we find that 5%, 10%,

13%, and 14% of the total scattered radiation is scattered in the forward direction between 0.5° and 2° . This results in a total positive bias due to the use of this particular FOV instead using an exact 0.5° FOV of 1.3%, 2.2%, 2.8%, and 2.5% for the respective wavelengths.

The second case considers small particles with weaker forward scattering peak but stronger wavelength dependence, which can be typical for background mineral dust, soot, etc. For this scenario we assumed an optical depth of 0.7, 0.5, 0.3, and 0.1 at the respective wavelengths 300, 500, 700, and 900 nm. The phase function for this case is also from Köpke *et al.* [1997]. An analysis similar to that discussed above for the first case suggests a positive bias in the direct beam irradiances of 3%, 0.8%, 0.3%, and 0.1% at the wavelengths 300, 500, 700, and 900 nm, respectively.

Aerosol optical thickness change $\Delta\tau$ is derived by applying the Bouguer-Lambert law to the direct beam through the pristine (pri) and the polluted (pol) air masses:

$$I_{\text{pri}} = I_0 e^{-\tau_{\text{pri}}} \quad (1)$$

$$I_{\text{pol}} = I_0 e^{-(\tau_{\text{pri}} + \Delta\tau)} \quad (2)$$

Rationing both equations yields an equation for $\Delta\tau$ which eliminates any dependency on the extraterrestrial solar irradiance I_0 and the absolute value of the optical depth τ for the pristine air.

$$\Delta\tau/\mu = -\ln(I_{\text{pol}}/I_{\text{pri}}) \quad (3)$$

$\Delta\tau$ depends only on the ratio of the direct irradiance measured during the reference day (I_{pri}) and the direct irradiance of the polluted day (I_{pol}). As a result, uncertainties in the extraterrestrial solar irradiance are factored out. Both are functions of the cosine of the solar zenith angle μ and the wavelength. I_{pri} has been derived using the data from day 78, plotting it versus μ , and fitting a straight line through all points for which $0.5 < \mu < 1.0$ is valid. This led to the following μ -dependent equation for I_{pri} on the reference day. As an example, for I_{pri} at 500 nm wavelength the following regression fit has been used:

$$I_{\text{pri}}(500) = 1.6853\mu + 0.23017. \quad (4)$$

However, applying this procedure to all wavelength bands of the spectroradiometer leads to a set of equations for I_{pri} , depending on wavelength and zenith angle of the sun.

We note from (2) and (3) that $\Delta\tau$ can potentially include changes in Rayleigh optical depth and ozone absorption (in spectral regions where applicable), both of which (as already discussed above) were found to be negligible. The time series of optical depth at five different wavelengths throughout the entire cruise is shown in Plate 3. The large data gap between day 66 and day 76 comes from crossing the ITCZ where the cloud cover did not allow any direct beam measurements and from the 4-day stay in Port Louis, Mauritius. The data between days 55–65 and 81–87 originate from north of the ITCZ. Data from south of the ITCZ could only be taken on three adjacent days, between days 76 and 78 (compare Figure 1). Day 78 is the reference day for the calculation of $\Delta\tau$. We restrict our attention to μ values between 0.5 and 1.0, because of the large cosine response errors for $\mu < 0.5$ (see Figure 6). Furthermore, in section 5 we will be normalizing τ and irradiances with μ , and this normalization procedure is not very effective for $\mu < 0.5$.

Plate 4 displays the latitudinal cross section of the optical depth $\Delta\tau$. The lowest values of $\Delta\tau$ occur only south of the ITCZ (at $\sim 11^\circ\text{S}$, on reference day 78). Most of the higher values are from north of the ITCZ where the influence of the Indian subcontinent is still very strong. The increasing values of $\Delta\tau$ between 15° and 20°S are most likely the influence of Madagascar, which may be adding aerosols to the upper layers. The optical depths increase monotonically as we approach the coast of India. Similar patterns of north-south gradient in optical depth have been observed during pre-INDOEX cruises undertaken in 1996 [Jayaraman *et al.*, 1998]. The wavelengths in Plate 3 have been chosen to fall within intervals with only little or no atmospheric absorption.

5. Spectral Forcing Efficiency

Here we relate $\Delta\tau$ to changes in irradiance. The procedure involves two steps.

1. First, we normalize both τ and the irradiance F , with μ . Ideally, we should relate τ directly to F , for each value of μ . For such a procedure to be statistically significant we need a large range of τ (~ 0.1 to 0.4 at least) for each value of μ . However, we do not have adequate samples within each bin of μ . On the other hand, by normalizing F with μ we are able to ensure adequate sample size for a statistically significant correlation between ΔF and $\Delta\tau$.

2. We relate the change in F from the reference value taken for the pristine day (F_{pri}) to the change in $\Delta\tau$ defined in section 4. The change in F is defined by

$$\Delta F(\lambda, \mu) = F_{\text{poi}}(\lambda, \mu) - F_{\text{pri}}(\lambda, \mu). \quad (5)$$

F stands for all three: the global, the direct, and the diffuse, respectively. It has been derived for all wavelength bands of the spectroradiometer. The reference day global, direct, and diffuse irradiance has also been determined from linear fits through the straight lines of F_{pri} versus μ for all clear-sky data on day 78. With the above definitions the spectral forcing efficiency of the aerosol (E_f) is defined as

$$E_f = \frac{\Delta F(\lambda)/\mu}{\Delta\tau(500)/\mu}. \quad (6)$$

F , again, stands for global, direct, or diffuse irradiance. The diffuse irradiance is obtained by subtracting the direct beam

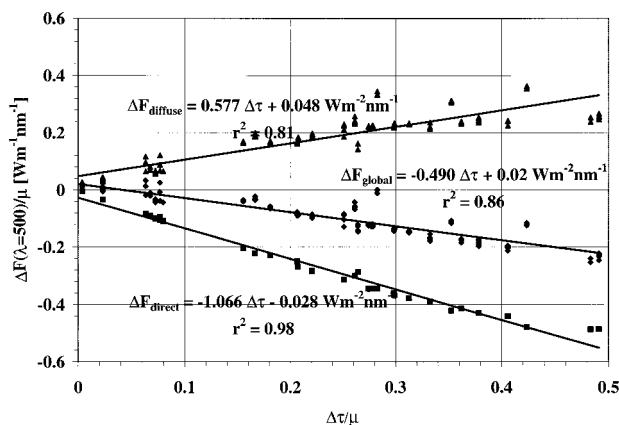


Figure 7. Change in global, direct, and diffuse irradiance at 500 nm, due to an increase in aerosol optical depth at 500 nm.

measurements from the global irradiance. Since we do not have simultaneous measurements of F and τ (they are separated by as much as 4 min), the synchronization had to be done using a time frame around the direct beam measurement and finding the next available global measurement. The time frame used here was set to be 3.5 min before and after the direct beam measurement. Since all data are normalized by the cosine of the solar zenith angle, the influence of varying the angle of incidence during these 7 min intervals is minimized. Figure 7 shows an example of scatterplots for the forcing at 500 nm for the global, direct, and diffuse components of light together with the appropriate values for the slopes.

The scatter, especially within the global and the diffuse data, comes from the fact that even though the direct beam could be taken frequently (through broken clouds even on cloudy days), there are only very few cases when the entire sky was completely cloudless. This results in variations in diffuse skylight due to reflection of cloud edges mostly near the solar disc or even partial coverage of the solar disc by very thin clouds shortly before or after the direct beam measurement.

Plates 5a and 5b show plots of the slopes for the global, the direct, and the diffuse irradiance versus wavelength derived from the entire data set. Maximum reduction of solar irradiance can be ~ 460 nm with asymptotically decreasing values for longer and shorter wavelengths. This is mainly influenced by the shape of the solar spectrum. The strong reduction of the aerosol influence within the water vapor bands displayed in Plate 5a at ~ 680 – 740 nm, 820 – 840 nm, and 900 – 1000 nm is due to a combination of two factors: (1) The absorption within the strong water vapor bands is efficiently saturated, so that aerosols have only a marginal impact on the global fluxes, and (2) This is further exceeded by the anticorrelation of aerosol optical depth and the columnar water vapor content. High aerosol loads have only been measured far north of the ITCZ where the water vapor content was low.

In regions with high water vapor content, which was the case near the ITCZ, the air was very clean, and the aerosol optical depth was low. We observe even positive forcing for the direct beam and global irradiance within the water vapor absorption bands, because the changes in water vapor absorption are dominating the above-mentioned spectral regions and are anticorrelated with the aerosol optical depth. In Plate 5b we removed the water vapor spectrum and show the aerosol influence for the rest of the spectral regions.

Besides the high spectral resolution of the reduction in the solar irradiance due to aerosols the impact on the 400 – 700 nm region is an important quantity, since this is the wavelength band of the photosynthetically active radiation (PAR). The PAR and its change due to aerosols is very important regarding biomass production of phytoplankton in the world ocean, which is a leading factor for the global carbon cycle [Pinker and Laszlo, 1992]. Furthermore, Jayaraman *et al.* [1998] have estimated the forcing in the PAR region during a pre-INDOEX cruise in 1996. Figure 8 displays the reduction in the 400 – 700 nm region of the solar wavelengths (PAR channel of advanced very high resolution radiometer (AVHRR)). To get the actual forcing, it is necessary to multiply the displayed values of reduction with $(1 - \text{albedo})$. On an average, the albedo is $\sim 6\%$ for the 400 – 700 nm interval over the ocean [Briegleb *et al.*, 1986], resulting in a factor of 0.94 for the ocean surface. All values shown so far have been derived from daytime measurements and refer to noontime solar insolation. Hence the forcing efficiency of -84 W m^{-2} shown in Figure 8 is applicable

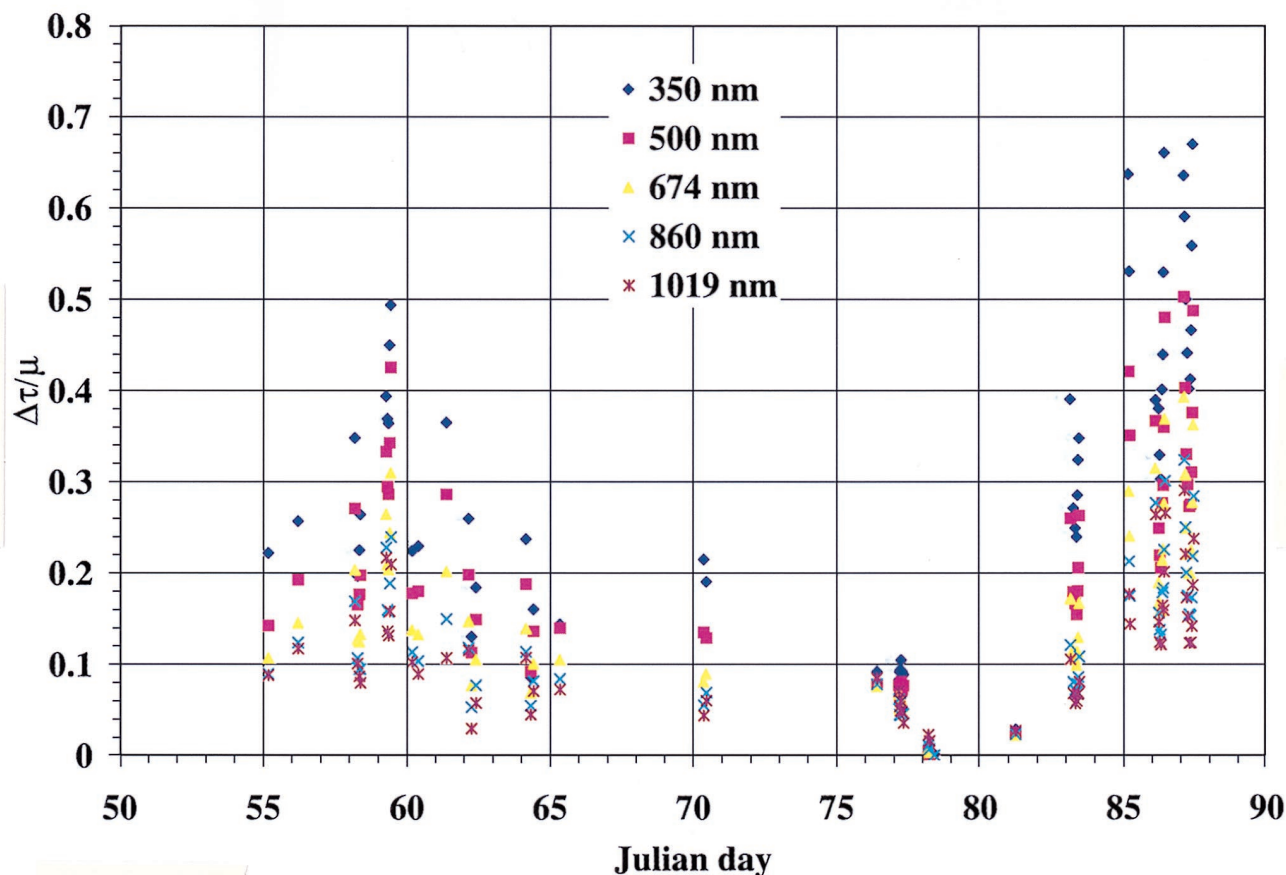


Plate 3. Time series of $\Delta\tau$ for five different wavelengths.

mainly for low solar zenith angles, (i.e., near-overhead sun) and should not be extrapolated to other sun angles. From their shipborne radiometric measurements, Jayaraman *et al.* [1998] derive a surface forcing efficiency of -80 to -117 W m^{-2} for similar solar angles.

6. Conclusion and Discussion

The paper provides some of the first estimates of the spectral nature of how aerosols modulate the radiative flux absorbed by the ocean. Onboard calibration of the 512-channel spectroradiometer, careful characterization of the angular response of the instrument, and frequent monitoring of its temperature control enabled us to accomplish a relative uncertainty of $<2\%$ for the cruise data. Furthermore, our analytical procedure of estimating the aerosol forcing as a change from reference pristine data significantly reduces errors due to uncertainties in the absolute calibration. The principal findings are summarized as follows: (1) Transport of pollutants from the Indian subcontinent introduces a large north-south gradient in aerosol optical depth, in the tropical Indian Ocean, varying from ~ 0.5 at 500 nm wavelength to as low as 0.05 around 10° – 15°S . (2) The spectral variations of the aerosol optical depth from the ultraviolet to the near infrared suggest the importance of small particles in the radiative forcing. (3) A remarkable shift in the wavelength of maximum intensity is seen in the direct component of the irradiance by comparing the irradiance between pristine and polluted air masses. The aerosols shift this maximal intensity from 460 nm to 580 nm

wavelength. This introduces a much stronger influence of aerosols on shorter wavelengths. (4) The spectral response of the irradiance to the aerosol pollution and the aerosol forcing in the PAR channel reveal interesting features. The noontime overhead Sun aerosol forcing between 400 nm and 700 nm was found to be -84 W m^{-2} per unit optical depth increase. (5) In response to the north-south gradient in aerosol optical depth the noontime aerosol forcing changes from about -35 W m^{-2} in the northern Arabian Sea to as low as -7 W m^{-2} around 15°S .

The numbers presented here are applicable only for vertical column of aerosols over the Arabian Sea and the Indian Ocean for the period of time shown. However, not all of the aerosol optical thickness results from boundary layer transport from the Indian subcontinent. It has been observed occasionally that there was a decoupling of boundary layer aerosols and the optical depth observed. Evidence of this decoupling is given by backscatter lidar data taken from the same vessel (T. Rucker, personal communications, 1998). Furthermore, trajectory calculations give evidence that the origins of these air masses are the arid and semiarid regions of Arabia and Africa. This means that the composition of the upper layer aerosols is more likely dust particles than sulfate, soot, or others, as expected for the boundary layer aerosol coming from India. The next important step is to link the spectral fluxes and forcing to aerosol species and size distribution. Such an attempt was made during the INDOEX intensive field phase conducted between January and March 1999.

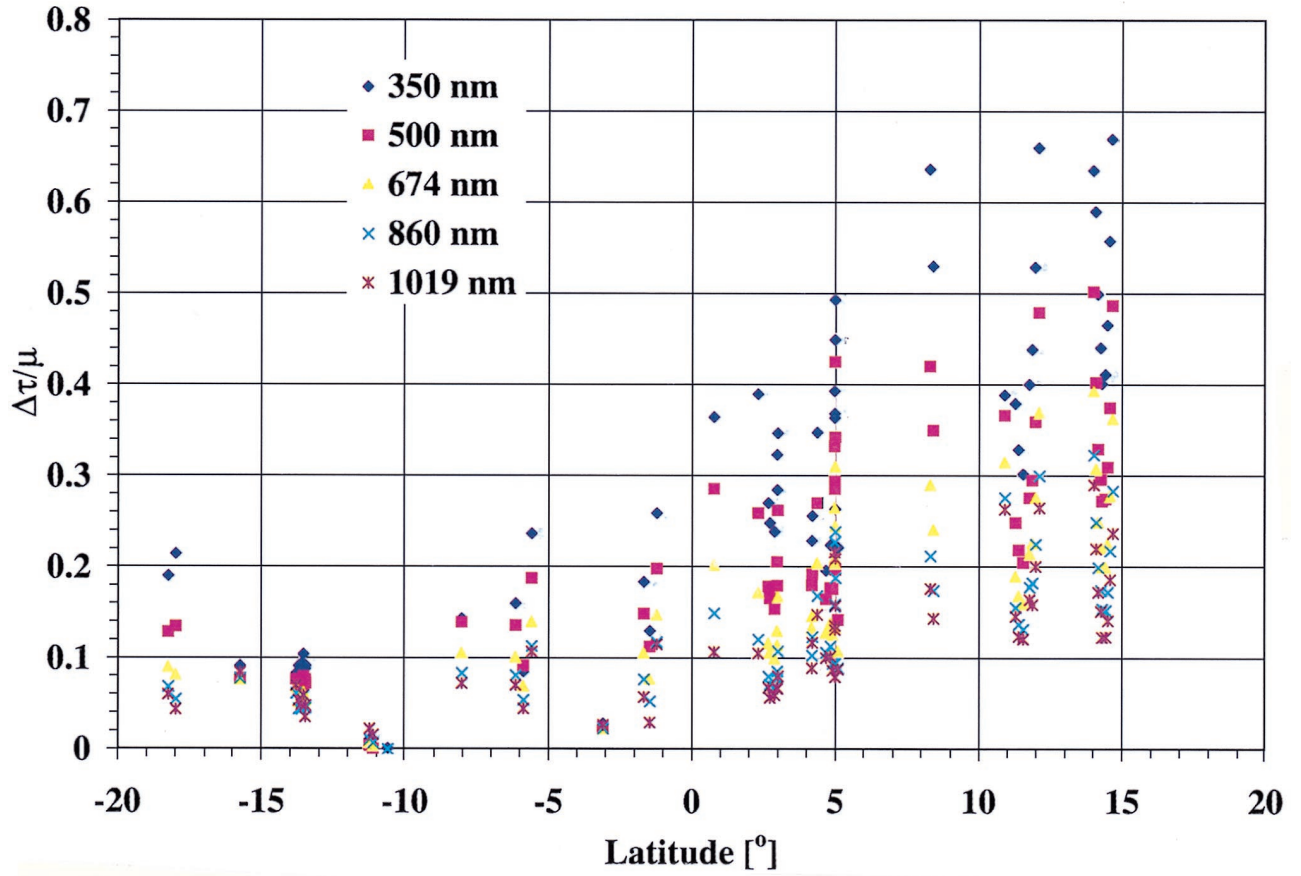


Plate 4. Latitudinal cross section of $\Delta\tau$ for five different wavelengths.

Appendix

The correction of the cosine response error was done making the following assumptions:

1. Since we are mostly interested in clear-sky global measurements, it is assumed that the diffuse skylight is isotropic. This assumption is not always true, especially when there are scattered clouds in the sky (see Plate 1). However, there is no other way to apply any correction. For the following reasons, problems arising from the anisotropy of the incident radiation field will only have a minimal impact on our results: (1) We restrict this study to clear skies; the cloud contamination is expected to be $<5\%$. (2) In spite of the great care with which we calibrated our measurement we do not use any particular data point in an absolute sense; we are only interested in the change in the global radiation due to changes in aerosol optical depth. Since we expect the anisotropy of clouds to change randomly from one measurement to another, its effect on the aerosol forcing estimate is expected to be minimal.

The diffuse portion of the global irradiance is the ratio between diffuse and global irradiance $(D(\lambda, \mu))/(G(\lambda, \mu))$. Multiplying $(D(\lambda, \mu))/(G(\lambda, \mu))$ by the mean cosine-weighted response error

$$\alpha(\lambda) = \int_1^0 \beta(\lambda, \mu) \mu d\mu \quad (7)$$

results in the correction factor to be applied to the measured global irradiance.

2. The second assumption is that only the direct solar beam

$(1 - (D(\lambda, \mu))/(G(\lambda, \mu)))$ introduces a significant deviation from the ideal cosine response to the global irradiance. Since the solar zenith angle is known, the angle-dependent correction $\beta(\lambda, \mu)$, as displayed in Figure 6, can be applied to the direct portion of the global irradiance once the ratio between diffuse and global radiation is known.

The following formula displays the applied cosine response correction for both the diffuse and direct beam portions:

$$G_{\text{cor}}(\lambda, \mu) = G_{\text{mea}}(\lambda, \mu) - G_{\text{mea}}(\lambda, \mu) \frac{D(\lambda, \mu)}{G(\lambda, \mu)} \alpha(\lambda) - G_{\text{mea}}(\lambda, \mu) \left[1 - \frac{D(\lambda, \mu)}{G(\lambda, \mu)} \right] \beta(\lambda, \mu), \quad (8)$$

or after some simple steps,

$$G_{\text{cor}}(\lambda, \mu) = G_{\text{mea}}(\lambda, \mu) \left\{ 1 - \frac{D_{\text{cal}}(\lambda, \mu)}{G_{\text{cal}}(\lambda, \mu)} \alpha(\lambda) - \left[1 - \frac{D_{\text{cal}}(\lambda, \mu)}{G_{\text{cal}}(\lambda, \mu)} \right] \beta(\lambda, \mu) \right\}. \quad (9)$$

The subscripts cor, mea, and cal stand for corrected, measured, and calculated, respectively. G is the global irradiance, and D is the diffuse irradiance. They depend on the wavelength λ and the cosine of the solar zenith angle μ .

The ratio between direct and global irradiance, which is necessary to apply these corrections to the global irradiance, could have been estimated from the measurements. Since this would include the error itself, radiative transfer calculations

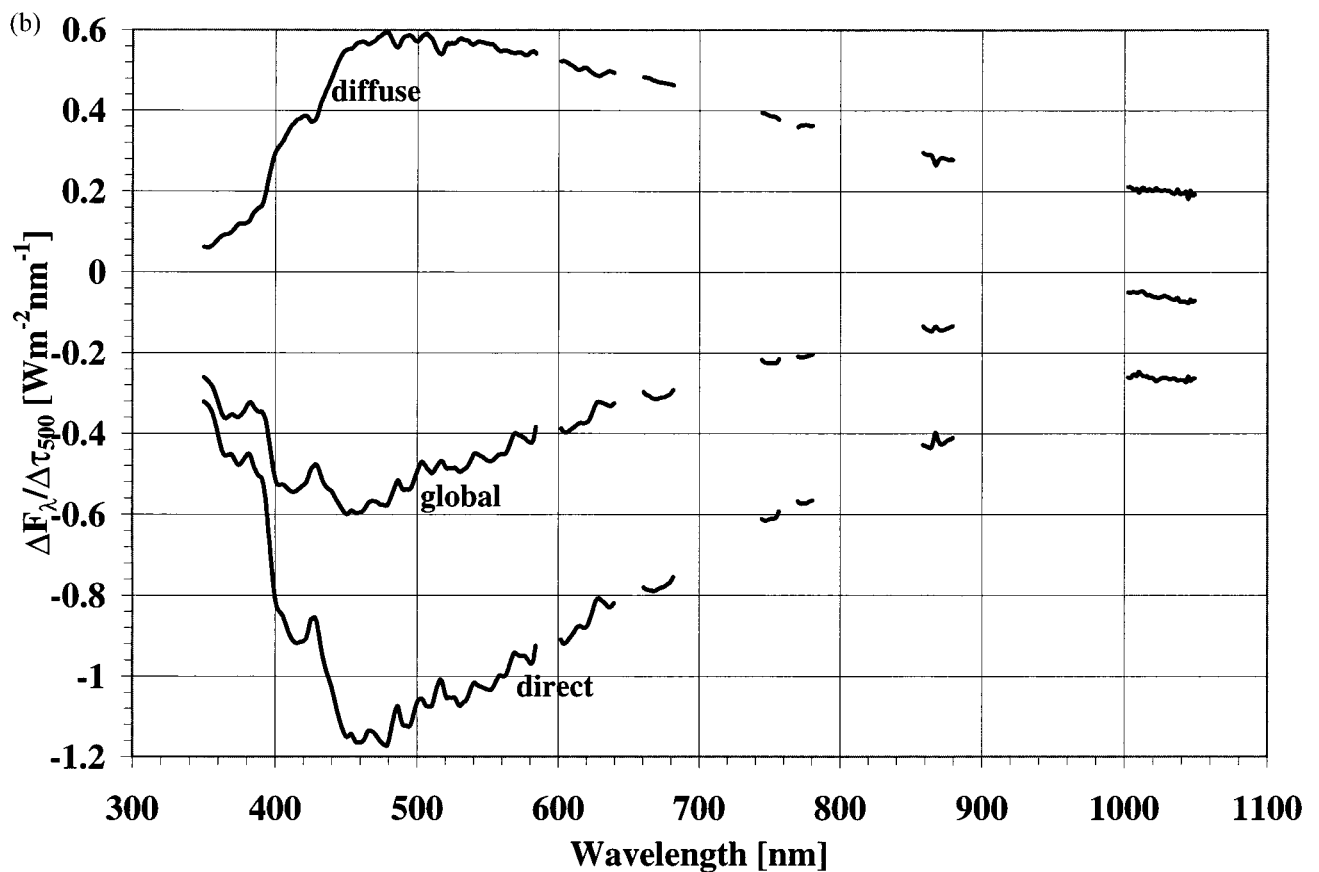
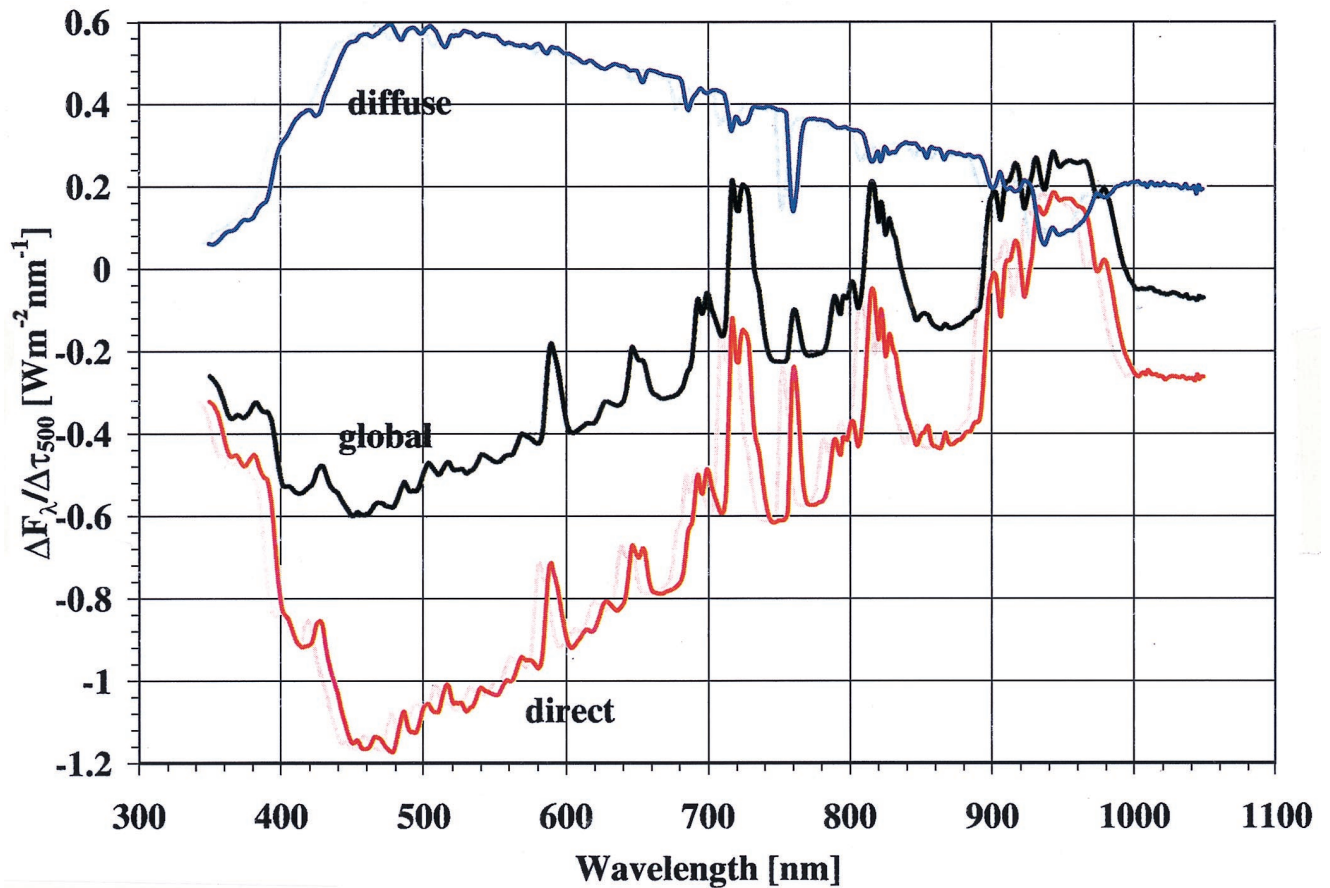


Plate 5. (a) $(\Delta F(\lambda)/\Delta \tau(500))$ between 350 and 1050 nm for the global, direct, and diffuse components of the irradiance. (b) Same as Plate 5a but without absorption bands of oxygen and water vapor.

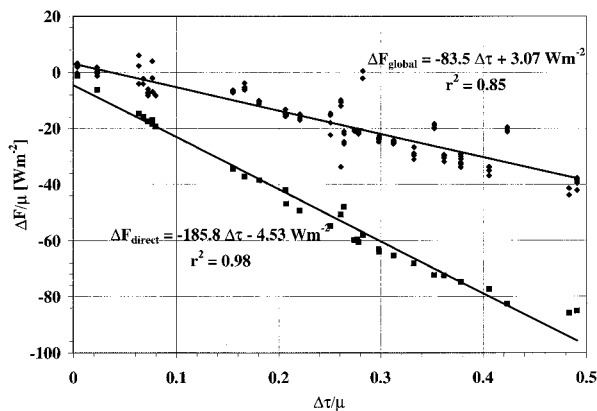


Figure 8. Scatterplot of the integrated 400–700 nm global forcing for noontime.

for clear sky with a typical aerosol optical depth of 0.15 of a polluted maritime type aerosol, after Köpke *et al.* [1997], have been used to estimate the ratio between global and diffuse irradiance for clear skies. These ratios vary with aerosol optical properties and wavelength as well as with solar zenith angle. The ratios between global and diffuse irradiance have been derived for all spectral channels and solar zenith angles.

For the fixed typical aerosol type described above, this correction varies with solar zenith angle and wavelengths. Typical values for this correction range from -0.3% at 1000 nm for overhead Sun to -10.5% at 600 nm for $\mu = 0.5$.

Acknowledgments. We thank A. P. Mitra, the National Institute of Oceanography at Goa, India, and the crew of the *Sagar Kanya* for making this cruise possible. The authors also wish to thank Francisco Valero and Sabrina Simpson of the Atmospheric Research Laboratory, Scripps Institution of Oceanography, University of California, San Diego, for facilitating the use of the calibration laboratory for the angular calibration of the instrument. This work was funded by the National Science Foundation (grant ATM9612887) and the Department of Energy (grant DE-FGO 3-91ER61198). This constitutes INDOEX publication 22 and C4 publication 205.

References

- Briegleb, B. P., P. Minnis, V. Ramanathan, and E. Harrison, Comparison of regional clear sky albedos inferred from satellite observations and model computations, *J. Clim. Appl. Meteorol.*, 25, 214–226, 1986.
- Curtiss, B., and A. F. H. Goetz, Field spectrometry: Techniques and instrumentation, in *FieldSpec User's Guide*, pp. 45–62, appendix A, Anal. Spectral Devices, Inc., Boulder, Colo., 1997.
- Intergovernmental Panel on Climate Change (IPCC), *Climate Change, 1994: Radiative Forcing of Climate Change and an Evaluation of IPCC IS92 Emission Scenarios*, 339 pp., Cambridge Univ. Press, New York, 1995.
- Jayaraman, A., D. Lubin, S. Ramachandran, V. Ramanathan, E. Woodbridge, W. Collins, and K. S. Zalpuri, Direct observations of aerosol radiative forcing over the tropical Indian Ocean during the January–February 1996 Pre-INDOEX cruise, *J. Geophys. Res.*, 103(D12), 13,827–13,836, 1998.
- Kiehl, J. T., and B. P. Briegleb, The radiative roles of sulfate aerosols and greenhouse gases in climate forcing, *Science*, 260, 311–314, 1993.
- Köpke, P., M. Hess, and I. Schult, Global aerosol data set, *Rep. 243*, Max-Planck-Inst. für Meteorol., Hamburg, Germany, 1997.
- Krishna Moorthy, K., S. K. Satheesh, and B. V. Krishna Murthy, Characteristics of Spectral Optical Depths and Size Distributions of Aerosols over Tropical Oceanic Regions, *J. Atmos. Sol. Terr. Phys.*, 60, 961–972, 1998.
- LI-COR, 1800-02 optical radiation calibrator: Instruction manual, *LI-COR Publ. 8508-44*, Lincoln, Nebr., 1990.
- Pham, M., G. Megie, G.-F. Müller, G. Brasseur, and C. Granier, 1995: A three-dimensional study of the tropospheric sulfur cycle, *J. Geophys. Res.*, 100(D12), 26,061–26,092, 1995.
- Pilewskie, P., A. F. H. Goetz, D. A. Beal, R. W. Bergstrom, and P. Mariani, Observations of the spectral distribution of solar irradiance at the ground during SUCCESS, *Geophys. Res. Lett.*, 25, 1141–1144, 1998.
- Pinker, R. T., and I. Laszlo, Global distribution of photosynthetically active radiation as observed from satellite, *J. Clim.*, 5, 56–65, 1992.
- J. Meywerk and V. Ramanathan, Center for Clouds, Chemistry, and Climate (C⁴), Center for Atmospheric Sciences, Scripps Institution of Oceanography, University of California, San Diego, 9500 Gilman Drive, La Jolla, CA 92093-0230. (jens@fiji.ucsd.edu)

(Received November 11, 1998; revised May 25, 1999; accepted June 22, 1999.)